

Research Article

Describing the Full Pore Size Distribution of Tight Sandstone and Analyzing the Impact of Clay Type on Pore Size Distribution

Qiang Lei ¹, Liehui Zhang,¹ Hongming Tang,¹ Yulong Zhao,¹ Man Chen,² and Chunyu Xie²

¹State Key Laboratory of Oil and Gas Reservoir Geology and Exploitation, Southwest Petroleum University, Chengdu 610500, China

²Southwest Oil & Gas Field Company, PetroChina, Chengdu, Sichuan 610041, China

Correspondence should be addressed to Qiang Lei; leiqiang050@163.com

Received 21 May 2019; Revised 13 June 2020; Accepted 1 July 2020; Published 15 September 2020

Academic Editor: Paola Cianfarra

Copyright © 2020 Qiang Lei et al. This is an open access article distributed under the Creative Commons Attribution License, which permits unrestricted use, distribution, and reproduction in any medium, provided the original work is properly cited.

Understanding the pore size distribution (PSD) of tight sandstone and the effect of clay minerals on the PSD is important for reservoir evaluation. Due to the complex shape of clay minerals, the multiscale pore size of tight sandstone, and the limitation of different experimental methods, it is hard to characterize the full PSD of tight sandstone, especially the point of connection (POC) of different derived PSD curves. In this paper, a more comprehensive technique integrated different precision methods of N₂/CO₂ low-pressure adsorption isotherms (N₂/CO₂-LPAI), mercury injection capillary pressure (MICP), nuclear magnetic resonance (NMR), and synchrotron X-ray computed tomography (XCT) to investigate the full PSD for three typical tight sandstones in China. Two different forms of PSD data presentations, differential pore volume versus diameter (dV/dR) and the log differential pore volume versus diameter (dV/dlogR), were firstly used to determine the POC. The full integrated PSD curves and scanning electron microscopy (SEM) images were carried out on the different clay-rich tight sandstones. The results show that the pores are classified into three types: intercrystalline pores (less than 0.01 μm), clay-related pores and residual intergranular pores (0.01 μm to 10 μm), and microfractures and dissolution pores (greater than 10 μm). The percentage of intercrystalline pores has a small relation on the porosity and connectivity, while there is a strong correlation among microfractures, dissolution pores, porosity, and especially connectivity. The microfractures and dissolution pores are the main connection channels, so a little change of the main connection channels will have a great effect on the permeability of the tight sandstones.

1. Introduction

Technological advances and energy demands have made tight sandstone reservoirs worth to be exploited [1, 2]. Tight reservoirs are characterized by low porosity and permeability and strong heterogeneity, especially considering the extensive development of nanometer-scale pore throats or the wide-ranging PSD [3–8]. Previous studies reveal that the PSD and pore-throat structure have a more direct effect on the storage and transport performance of tight sandstone reservoirs than porosity and permeability [9, 10]. Different PSD and pore throat structures have different percolation mechanisms, which control the form, transportation, gathering, and recovery of tight gas and oil [11]. Therefore, research on the pore structure characteristics in tight sandstone reservoirs is necessary [12–15].

To characterize the complex pore structure and PSD of tight sandstone, three types of techniques are widely used [16, 17]: (1) methods involving penetration fluids, including MICP and N₂/CO₂-LPAI [18–21]; (2) nondestructive physical techniques, including NMR [22, 23]; and (3) and microscopic imaging, such as SEM [24, 25] or XCT [26]. Although these methods are widely used, they have many limitations. In the PSD curves derived by MICP, the size of these pores is controlled by the corresponding throats, and the minimum pore size relies on the maximum pressure of the mercury injection apparatus. To reach the nanopores in tight sandstone, a high injection pressure is necessary, but if the pressure is too high, the core may incur microfractures, which will affect the accuracy of the data. Therefore, MICP is accurate only for pore throats larger than 15 nanometers in tight sandstone [27–31]. For N₂-LPAI, at relative pressure

greater than 0.45, capillary condensation in mesopores and macropores occurs according to the Kelvin equation, and the PSD can be calculated by the Barrett-Joyner-Halenda (BJH) method [32–36]. However, this method cannot describe micropores and narrow mesopores due to the correlation between the aperture of these pores and relative pressure is poor. [37, 38]; furthermore, the physical phenomena (like the tensile strength effect, adsorbate phase transitions, and monolayer formation) will affect the accuracy in micropores (<2 nm) and some mesopores (2 nm to 10 nm) calculated by the BJH method, so the assessment of the BJH method for pore size calculations in tight sandstone is inadequate [39].

Due to the relatively high boiling point (273.1 K) and high saturation vapor pressure (3.5 MPa) of CO₂, it is easy for its molecules to enter the pores narrower than 2 nanometers [40, 41]. In the density functional theory (DFT) approach, adsorption isotherms in model pores are calculated by the intermolecular potentials of the fluid–fluid and solid–fluid interactions. According to the DFT, there are two main improved methods: the nonlocal density functional theory (NLDF) and the local density functional theory (LDFT). The NLDF method is more accurate to describe the thermodynamic state of fluids in the micropores, and it was recommended by the International Organization for Standards (ISO) [42]. Unlike other methods, which can only calculate the micropores (Horvath-Kawazoe method) [43] or mesopores (BJH method) [32], NLDF can describe micro- and mesopores simultaneously. However, the accuracy of the NLDF method depends on the effect of the fluid molecules in the pores, for example, the size of the fluid molecule can affect the minimum pores calculated by NLDF, and the interaction parameters between fluid and solid, and many researchers have improved the NLDF theory and used the method to accurately analyze the PSD of nanopores [44–47].

NMR can be applied to the study of conventional reservoirs and unconventional resources (such as coal, shale, and tight sandstone), using the relaxation time of fluid in porous materials to characterize the PSD [23, 48–53]. However, the probe liquid has a great impact on the relaxation time for the NMR due to the fluid properties and whether the probe liquid can enter the pore space [54]. In addition, the conversion of the NMR relaxation time into pore size depends on a conversion coefficient called surface relaxivity, which relates to the relaxing strength of the pore surface (i.e., the mineral surface of grains), and is usually determined with the help of other experimental methods, especially the MICP [55, 56]. Nondestructive synchrotron small-angle X-ray scattering (XCT) provided a three-dimensional visualization method to investigate the nanopores and micropores [57, 58]. With a 3D reconstruction from XCT images, porosity can be calculated by counting voxels, and the PSD and connectivity can be represented by a cylinder network and stick-and-ball network [59–62]. Theoretically speaking, XCT can describe any pores, but this technology is limited by a small field of view (FOV), and the image area is inversely proportional to image resolution, which means that high resolution can only describe small-scale pores, whereas low resolution can only describe large-scale pores.

Due to the wide range of pore sizes in tight sandstone reservoirs, from nanometers to micrometers, none of the above methods can characterize the entire PSD in tight sandstone alone [63]. The integration of multiple methods is an effective way to solve this problem [64, 65]. Previous researchers only integrated a few methods, which is insufficient for the full PSD of tight sandstone [21, 30, 64]. This study used multiple methods (including N₂-LPPI, MICP, NMR, XCT, and NLDF) to get the PSD curves of core samples from three sedimentary basins. A new integrated method was firstly used to determine the more accurate POCs between different derived PSD curves. And then, the full PSDs are classified into three types: intercrystalline pores, clay-related pores and residual intergranular pores, and microfractures and dissolution pores, and we investigate the pore types in different clay-rich tight sandstones and the relationship between the pore type and porosity and permeability.

2. Materials and Experiment Methods

2.1. Samples. Seven tight sandstones were collected from three different reservoirs: sample 904 and 905 were drilled from the borehole in the Bashijiqi formation of the Kuqa depression in the Tarim Basin; samples 118, 119, and 120 were drilled from the outcrop in the Xujiahe formation which was in West Sichuan depression; and samples 4 and 264 were drilled from the borehole in the 8th member of the Upper Paleozoic Shihezi formation of the Sulige gas field in the Ordos basin. And a geological map with all samples position is shown in Figure 1. The Bashijiqi formation is the main gas reservoir in the Kuqa depression, which is found in a typical deep-seated, anticlinal structural trap [66]. The Bashijiqi formation is mainly composed of brown fine-grained fibrous illite-rich quartz sandstone [67]. The main sedimentary facies of the Xujiahe formation in the West Sichuan depression is the delta front. The formation is mainly composed of green lithic quartz sandstone and contains abundant chlorite. Due to the ubiquity, distribution, and morphology of the chlorite, the porosity of this formation is abnormally high [68]. The 8th member of the Upper Paleozoic Shihezi formation is the main gas reservoir of the Shihezi formation, and this formation is dominated by lithic quartz sandstone with a large quantity of kaolinite. The intercrystalline pores and the dissolved intergranular pores are the main factors to improve the porosity and permeability in this formation [69].

2.2. Experimental Methods

2.2.1. Sample Preparation. Each sample was represented by a regular cylinder (approximately 5 cm long and 2.5 cm in diameter), drilled from a homogeneous section perpendicular to the bedding. All samples were dried at 100°C for 12 h in a vacuum oven; then, they were subjected to nitrogen permeability and porosity measurements using a CMS-300 automatic permeability measuring instrument (Core Laboratories: The Reservoir Optimization Company) (Table 1). The range of porosity for this apparatus is from 0.01% to 40% and the permeability is from 0.00005 mD to 15D; meanwhile, this

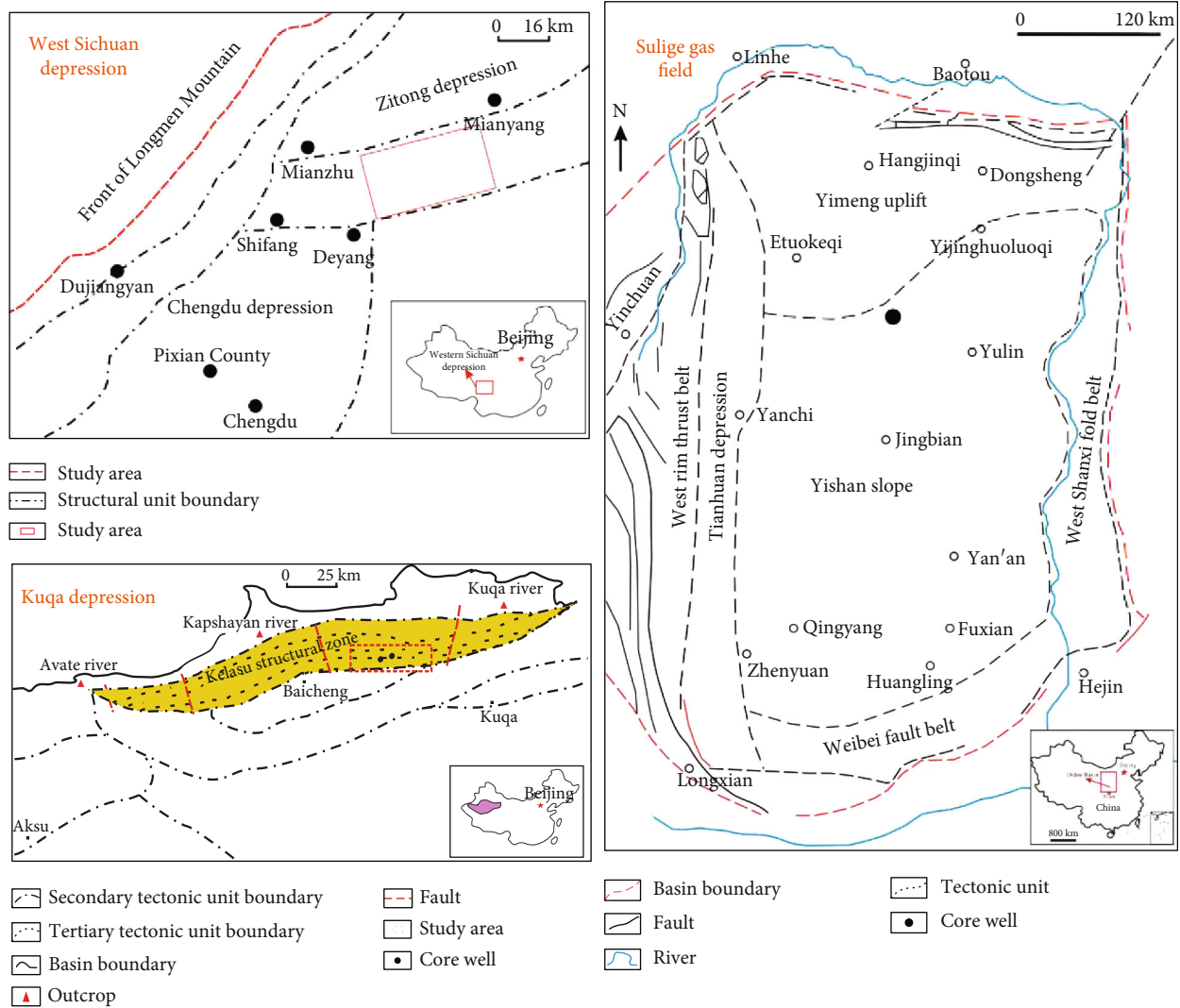


FIGURE 1: Location of the study area and the core wells in three different reservoirs.

TABLE 1: Petrophysical parameters and mineral compositions of the seven tight sandstones.

Sample	4	264	904	905	118	119	120	
Depth (m)	2796.37	3014.56	7870	7902.29	\	\	\	
Porosity (%)	6.93	6.31	4.47	5.68	16.51	16.69	16.58	
Permeability (mD)	0.019	0.035	0.001	0.008	0.175	0.166	0.201	
Content of mineral component from XRD	Quartz (%)	82.3	77.83	63.27	70.72	55.97	48.28	49.64
	K-feldspar (%)	0.34	0	5.65	2.35	0.86	1.4	6.57
	Anorthoclase (%)	7.94	0	16.23	9.56	26.44	31.15	29.05
	Calcite (%)	0	5.21	0	0	0	0	0
	Dolomite (%)	0.69	0	3.8	14.73	2.79	3.55	1.54
	Siderite (%)	0	1.49	0	0	0	0	0
	Pyrite (%)	0	0	2.05	0.07	0	0	0
Content of clay from XRD	Illite (%)	0	0	3.62	1.69	0	0	0
	Chlorite (%)	0	0	0	0	12.65	10.56	11.08
	Kaolinite (%)	5.25	12.64	0	0	0	0	0

instrument is especially suitable for testing low-permeability samples like tight sandstones which does not comply with Darcy's law.

2.2.2. NMR Test. These samples were then saturated with the NaCl solution at 40 MPa pressure for 24 h to avoid clay swelling; then, NMR measurements were taken using a MacoMR12-150H-I (Suzhou Niumag Analytical Instrument Co., Ltd.), with a resonant frequency of 11.825 MHz using a standard Carr-Purcell-Meiboom-Gill pulse sequence with an echo number of 18,000 over a wait time of 3000 ms and cumulative sampling frequency of 64.

2.2.3. MICP Test. Approximately 2 cm long parts were cut from the seven samples for the MICP measurement. The MICP experiment was carried out with an AutoPore IV 9505 porosimeter (Micromeritics Instrument Ltd.) in the Daqing Oilfield Laboratory in China. Before the analysis, tight sandstones were dried at 100°C for at least 12 h in a vacuum oven again to avoid the effect of residual water when cutting the cores. The MICP maximum intrusion pressure was 100 MPa, corresponding to a pore throat radius of approximately 7 nm.

2.2.4. N₂-LPAI Test. The remaining parts were cut into two parts (2 cm and 1 cm long); the 2 cm parts were broken into pieces (60–80 mesh) and degassed in the vacuum oven for 14 h at 220°C to remove any adsorbed water and gas. Then, these broken pieces were used for N₂-LPAI with a NOVA 2000e apparatus (Quantachrome Instruments) at the Southwest Petroleum University of China.

2.2.5. CO₂-LPAI Test. The broken pieces (60–80 mesh) were degassed in the vacuum oven for 10 h at 110°C to remove any adsorbed water and gas. And then, degassed samples were subjected to CO₂ adsorption measurement with a constant temperature of 0°C and a relative pressure between 0 and 0.35, and 40 adsorption points are selected during the measurement. The experiment is measured by a 3H-2000PS1 apparatus (BeiShiDe Instrument) in Dalian Ekeyan Company of China.

2.2.6. X-Ray Diffraction Test. These pieces after the CO₂-LPAI test were cut for X-ray diffraction (XRD) to determine the mineral composition of the samples and the clay mineralogy (Table 1). These pieces were soaked with deionized water for 24 h to extract the clay minerals, and these extracted clay minerals were prepared on glass slides and XRD test. The type of minerals was identified from the position of peaks and its intensities by using the professional software X'Pert High Score Plus. And all steps followed the Chinese oil and gas industry standards SY/T 5163-2010 [70].

2.2.7. XCT Test. Cylinders (diameter of 6 mm) were drilled from the 1 cm long parts for the XCT test. The XCT was performed with a MICROXCT-400 X-ray microscope (Carl Zeiss Optics Co., Ltd.) in Southwest Petroleum University of China. The highest spatial resolution of this apparatus is 1 μm/pixel, and the maximum power of the X-ray source is 10 W and the maximum allowable voltage is 140 kV.

2.2.8. SEM Test. The remaining parts after the XCT testing were used to measure the SEM by FEI Quanta 650 FEG apparatus (FEI Company, USA). This apparatus has two different modes. Under a highly vacuumed environment, the highest resolution of this apparatus is 1 nm/pixel, and under a low vacuumed environment, the resolution of the apparatus is 1.4 nm/pixel. In this study, we focus on analyzing the SEM images of the sample surface that has been polished with argon ion beams and the fresh section of the same sample.

3. Results

3.1. Petrophysical Characteristics of the Samples. The porosity, permeability, and mineral component contents of the seven samples are presented in Table 1.

To analyze the important characteristic main clay mineral in different samples, only the content of the main clay mineral determined by XRD is shown the Table 1. There is no obvious relationship among permeability, porosity, and the content of clay minerals. We cannot ascribe the pore structure of tight sandstones to the content of clay minerals only, and we should pay more attention to the shape and types of clay minerals.

Looking at the SEM images in Figure 2 and the clay content in Table 1, all the samples can be classified into three types: illite-rich samples, kaolinite-rich samples, and chlorite-rich samples. Due to the effect of the clay minerals, the main pore types of different samples can be divided into five types: intercrystalline pores, dissolution pores, microfractures, clay-related pores, and residual intergranular pores. The pores in the kaolinite-rich samples are mainly intercrystalline pores and dissolution pores, the pores in the illite-rich samples are mainly clay-related pores, and the pores in the chlorite-rich samples are mainly clay-related pores, microfractures, and residual intergranular pores.

The kaolinite mineral with well-defined crystal habit and morphology is called autochthonous kaolinite. There are two types of autochthonous kaolinite: one of the autochthonous kaolinites is formed from the feldspar dissolved by the acidic water, and this kind of autochthonous kaolinite is distributed on the feldspar surface; and the other autochthonous kaolinite is precipitated from pore fluids, and this kind of autochthonous kaolinite has a well-defined crystal structure and the form of this kaolinite aggregation appears wormlike and as booklets. The kaolinite from the Shihezi formation has a booklet morphology (Figures 2(b) and 2(d)), which belongs to the second kaolinite type, and it is regionally distributed (Figures 2(a) and 2(c)), and the pore types in this kind of samples contain intercrystalline pores, dissolution pores, and some intergranular pores.

Generally, the hydrolysis of the potassium feldspar and the conversion of montmorillonite can get the illite. The illite from the Bashijiqike formation is fibrous (Figures 2(f) and 2(h)) and is accumulated in the cleavages and weak ruptures of the potash feldspar (Figures 2(e) and 2(g)). This kind of samples is pretty tight and has poor porosity, and the main pore types are the intercrystalline pores and clay-related pores. SEM images from the Xujiahe formation indicate that the chlorite of this formation typically occurs as extensive

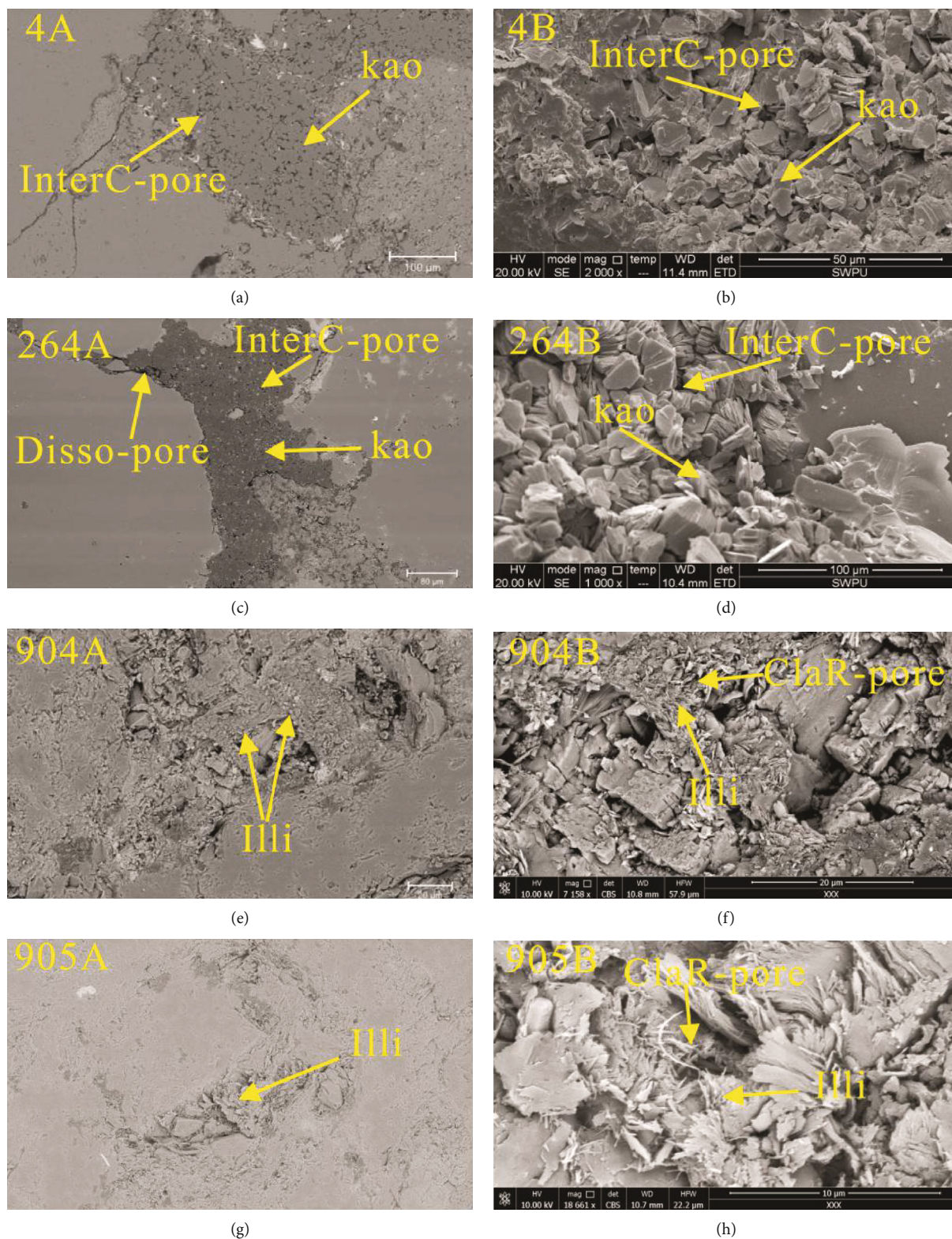


FIGURE 2: Continued.

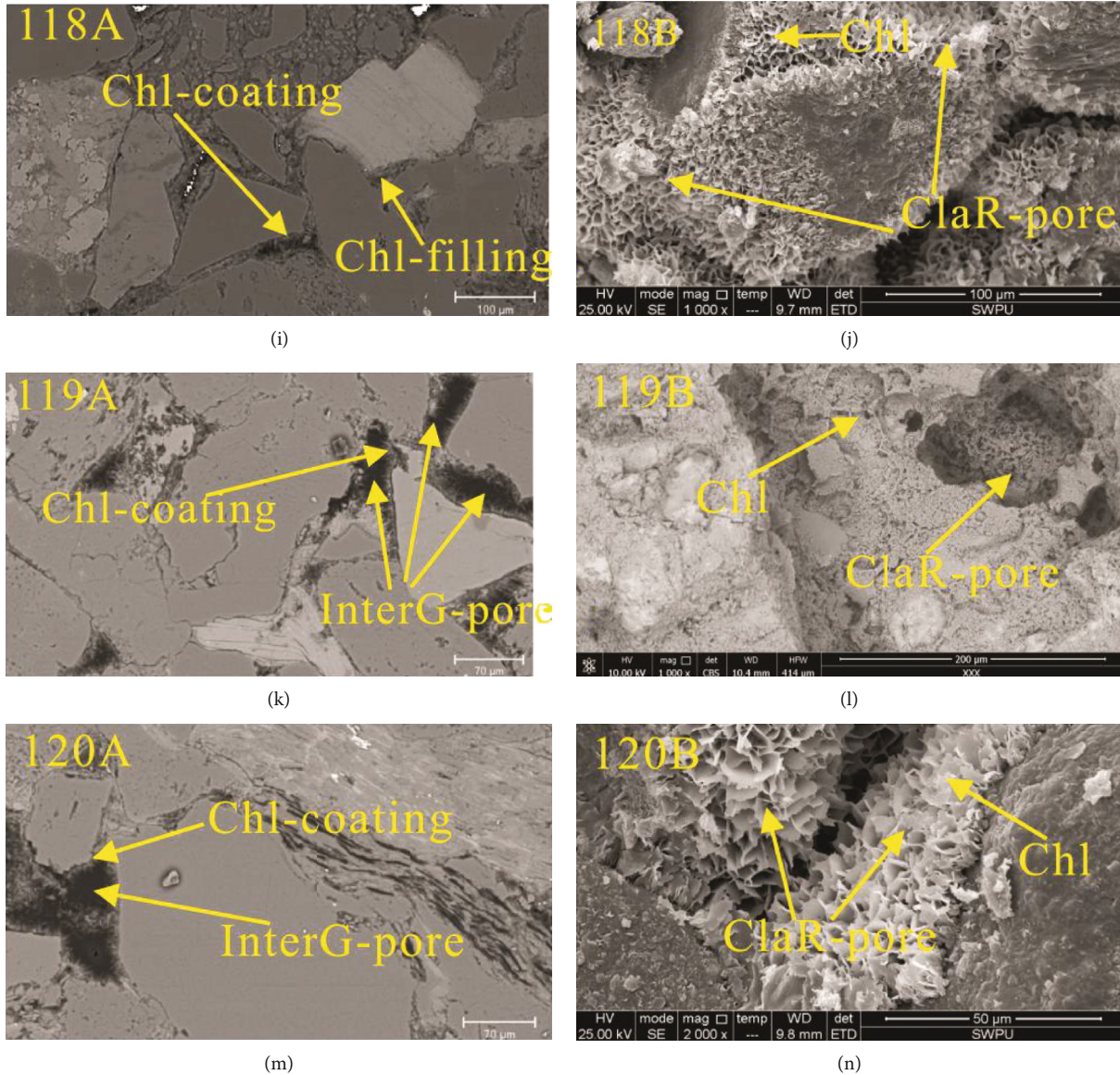


FIGURE 2: Typical clay and pore types identified by SEM images and backscatter images in tight sandstones. Chl: chlorite; Illi: illite; Kao: kaolinite; InterG: intergranular; Disso: dissolution; InterC: intercrystalline; ClaR: clay-related; micrF: microfractures.

grain coating (Figures 2(k) and 2(m)). The chlorite grew perpendicularly to the grain surface (Figures 2(j)–2(n)), and some of them will fill in the pore space (Figure 2(i)); meanwhile, the shape of chlorite is uniform when the pore fluids are alkaline. The pore types in this kind of samples contain clay-related pores and residual intergranular pores.

3.2. N_2/CO_2 -LPAI, MICP, NMR, and XCT Experiment Result.

The N_2 adsorption-desorption isotherms of samples were obtained at 77.3 K, and the relative pressure range is approximately 0.1–0.95. The PSD was calculated from the adsorption data at relative pressures greater than 0.45, when condensation appeared in the capillaries, using the BJH method [32, 33, 36]. All of the N_2 adsorption-desorption isotherms are type H3 based on the IUPAC [71]. The classification of the N_2 adsorption-desorption isotherm type is related

to an integrated pore shape. The hysteresis loops of N_2 adsorption-desorption isotherms are shown in Figure 3.

In the density functional theory approach, the local density of the adsorbate confined in a pore is calculated by minimizing the grand thermodynamic potential. Figure 4 shows the CO_2 adsorption isotherms, which begin at approximately $P/P_0 = 4.4 \times 10^{-5}$, but without a saturation plateau when $P/P_0 = 0.03$.

The mercury intrusion and extrusion curves of the seven samples obtained from the MICP test are shown in Figure 5. During the extrusion process, the capillary pressure resists the nonwetting mercury, leading to a hysteresis loop for each curve, indicating that some mercury is still trapped in some pore bodies.

The transverse relaxation time (T_2) distributions of the seven samples measured by NMR are shown in Figure 6.

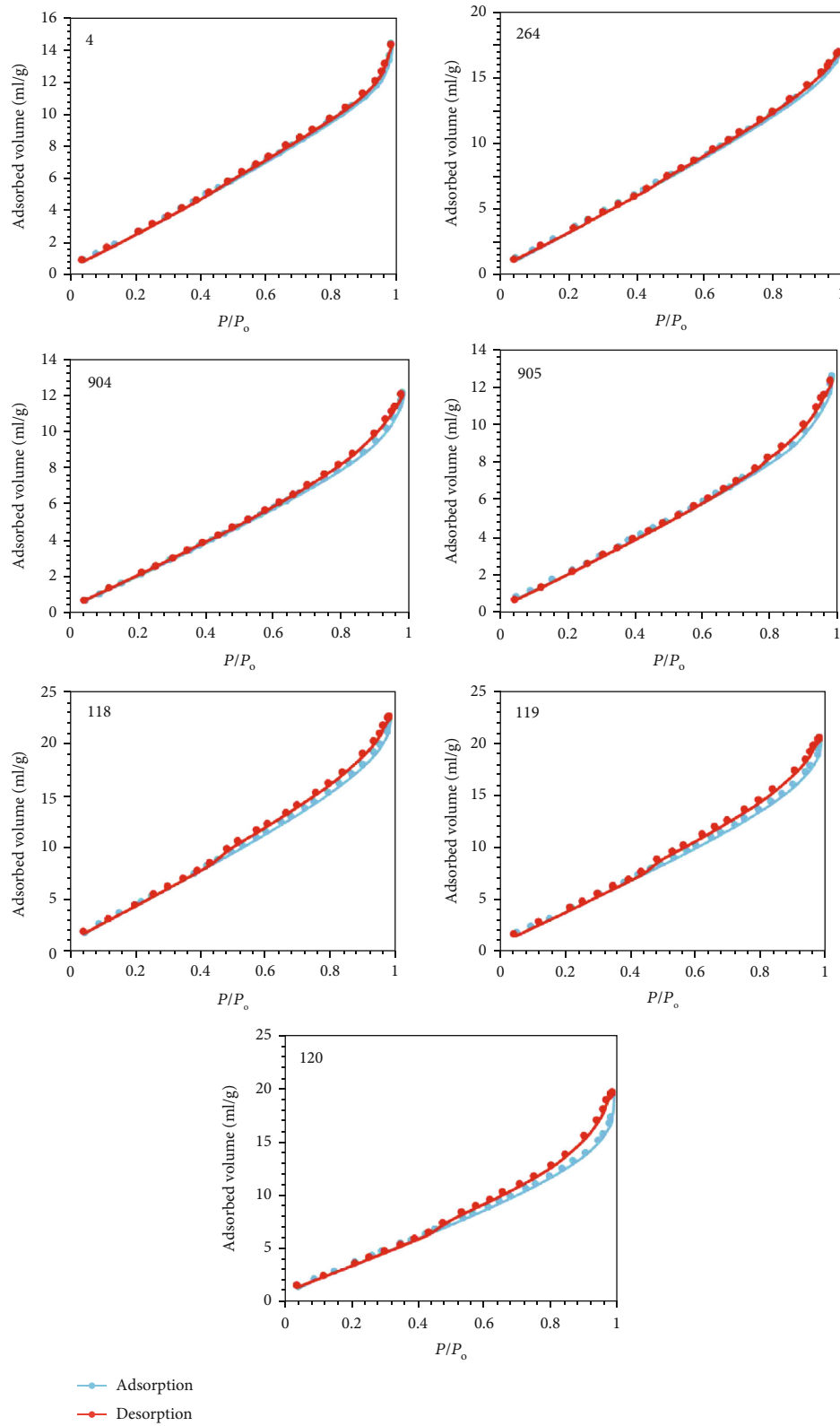


FIGURE 3: N_2 -LPAI hysteresis loops for the seven tight sandstones.

Generally, the amplitude, shape, and width of the T_2 distributions can qualitatively describe the volume, connectivity, and size of pores [72]. Samples 4, 264, 118, 119, and 120 have

the same T_2 distribution width but the amplitude of samples 4 and 264 is smaller than that of samples 118, 119, and 120 in the NMR, and samples 904 and 905 have the most narrow T_2

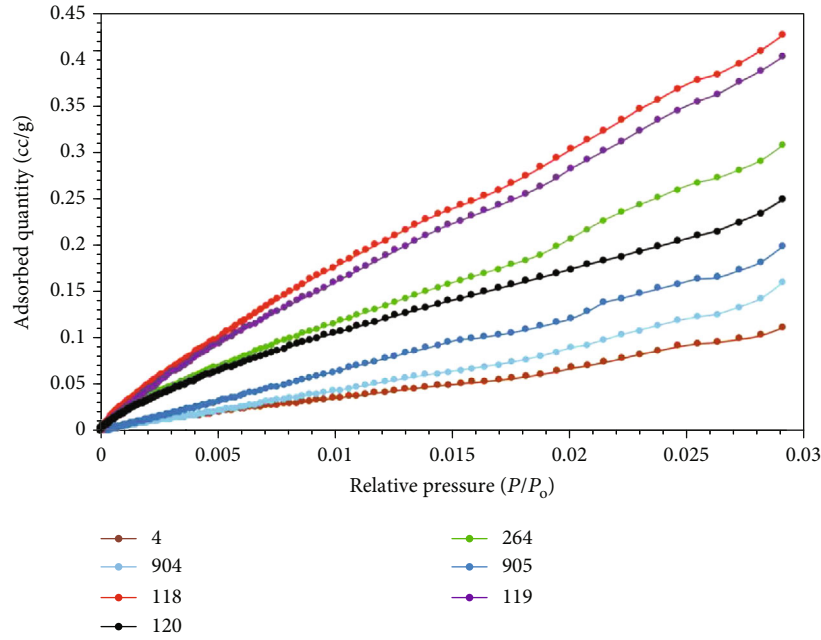


FIGURE 4: CO₂ adsorption isotherms for the seven samples.

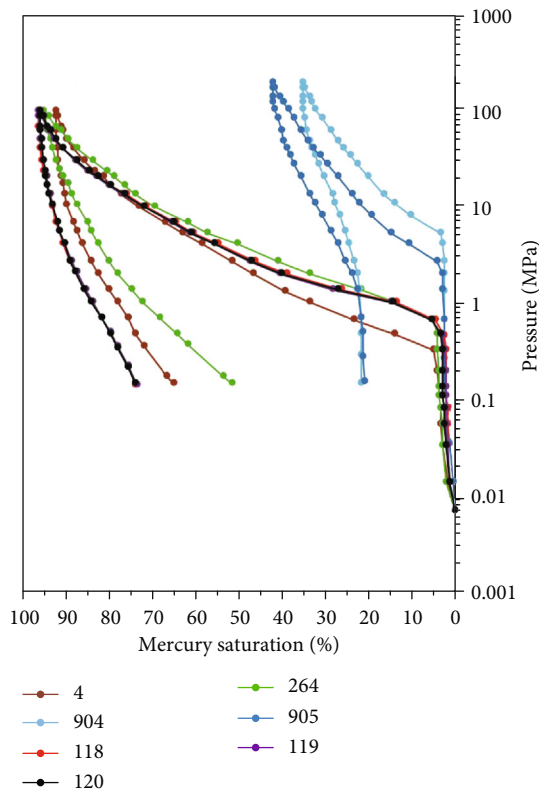


FIGURE 5: Mercury intrusion and extrusion curves for the seven samples.

distribution width and the smallest amplitude. The relationship between these characteristics shown in NMR and the porosity and permeability is obvious.

XCT is a nondestructive way to visualize the inner content of rock samples in three dimensions [73]. Two-

dimensional XCT images were created using the software PerGeos 1.5.0 with channel 1 and a pixel size of $2.065 \mu\text{m} \times 2.065 \mu\text{m} \times 2.065 \mu\text{m}$ for samples 4, 264, 904, and 905, and $4.249 \mu\text{m} \times 4.249 \mu\text{m} \times 4.249 \mu\text{m}$ for samples 118, 119, and 120. Stacking all the 2D XCT images, we can reconstruct a 3D visualization of the samples (Figure 7). Before pore space and mineral segmentation, the destriping filter algorithm is executed in order to remove the perpendicular curtaining irregularities arising during imaging. This algorithm increases the quality of subsequent porosity segmentation.

The whole 3D reconstruction samples were too large to calculate the pore structure parameters. Given the anisotropy and for the convenience of calculation, we should determine the representative elementary volume (REV), which is the minimum core volume to describe the petrophysical properties of the rock samples. Generally, we use the porosity of the core volume as a constraint boundary condition to make sure of the REV size. After that, we put the center of the coordinate in the 3D digital cores (top, center, and bottom of the 3D digital cores), and then slowly increased the length as a cube side length until the porosity in the cube is stable, and at this point, the side length of the cube is the REV size. Figures 8–10 show the relationship between the size of the cube and its porosity from directions of the top, center, and bottom, and the REV size is 300 pixels.

3.3. PSDs of Different Methods. The N₂-LPAI relies on the characteristics of the nitrogen adsorbing on the crushed samples to measure the specific surface area and PSD of the samples. The N₂ adsorption-desorption isotherms of samples were obtained at 77.3 K, and the relative pressure range is in 0.1–0.95. The PSD was calculated from the adsorption data in the relative pressure bigger than 0.45, when the condensation appears in the capillaries, by using the BJH method as follows [32, 33, 36]:

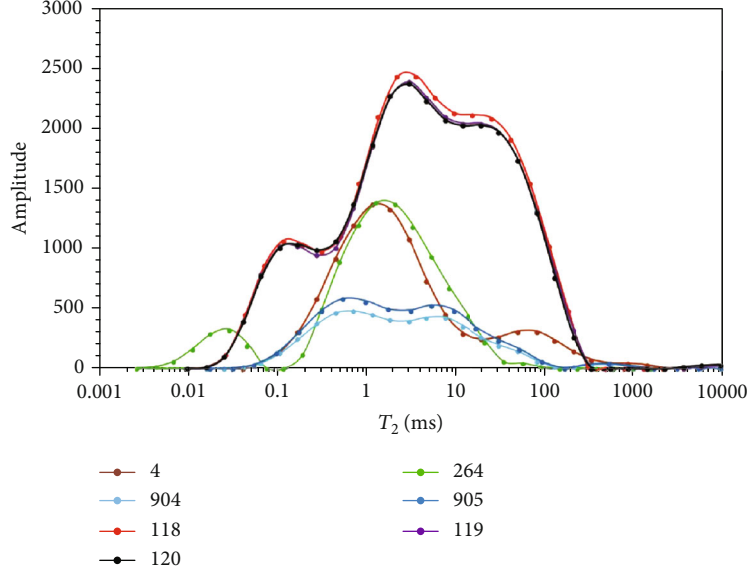


FIGURE 6: NMR T_2 distributions of the seven samples.

$$r = -2\gamma V_m / [RT \ln (P/P_o)] + 0.354[-5/\ln (P/P_o)]^{1/3}, \quad (1)$$

where r is the pore radius in nm, γ is the surface tension (8.88×10^{-3} N/m), V_m is the nitrogen molar volume (34.68 cc/mol), R is the universal gas constant (8.314 J/mol/k), T is the absolute temperature (77 k), and P/P_o is the relative pressure.

For the CO_2 -LPAI, the PSD is derived by the NLDFT method; the local density of the adsorbate confined in a pore is calculated by the minimization of the grand thermodynamic potential Ω :

$$\begin{aligned} \Omega[\rho(r)] = & F_{\text{HS}}[\rho(r)] + \frac{1}{2} \iint dr dr' \rho(r) \rho(r') \Phi_{\text{attr}}([r-r']) \\ & - \int dr \rho(r) [\mu - U_{\text{ext}}(r)], \end{aligned} \quad (2)$$

where $F_{\text{HS}}[\rho(r)]$ is the nonlocal free energy functional of hard spheres. The second term in the right-hand side is the mean field free energy due to the attractive interactions Φ_{attr} . And $U_{\text{ext}}(r)$ is the potential imposed by the pore wall. And we assume that $U_{\text{ext}}(r)$ refers mostly to the interactions of fluid molecules with the external cylindrical layer of oxygen atoms of the pore wall [74].

The excess adsorption per unit area of cylindrical pore can be calculated by the density distribution $\rho(r)$:

$$N_s(P/P_o) = \frac{2}{D} \int_0^{2/D} \rho(r) r dr - \frac{D_{\text{in}}}{4} \rho_g(P/P_o), \quad (3)$$

where $\rho_g(P/P_o)$ is the bulk gas density at the relative pressure, P/P_o , $D_{\text{in}} = D - \sigma_{\text{ss}}$ is the 'internal' pore diameter, D is

the center of oxygen atoms in the pore wall, and σ_{ss} is the effective diameter of oxygen.

The entry of nonwetting mercury has a surface tension as liquid; so, with different external pressure, it can get into the different sizes of the pore space, and the relation of intrusion pressure P_c with the pore throat radius r_c should satisfy the Washburn equation as follows [75]:

$$P_c = \frac{2\sigma \cos \theta}{r_c} = \frac{0.735}{r_c}, \quad (4)$$

where the interfacial tension σ and wetting angle θ are assigned as 0.48 J/m² and 140°, respectively.

NMR measurements can determine the PSD from the relationship between the distribution curve of transverse relaxation time and specific surface of the core [30]. The transverse relaxation comprises the bulk relaxation, surface relaxation, and diffusion relaxation, and the equation is as follows:

$$\frac{1}{T_2} = \frac{1}{T_{2B}} + \rho_2 \frac{S}{V} + \frac{D(\gamma C T_E)^2}{12}, \quad (5)$$

where the T_2 is the transverse relaxation time in ms, D is the diffusion coefficient, $\mu\text{m}^2/\text{ms}$; C is the internal field gradients, G/cm; T_E is the echo spacing, ms; S is the superficial area of the pore, cm^2 ; V is the pore volume, cm^3 ; and ρ_2 is the transverse surface relaxivity of the rock, $\mu\text{m}/\text{ms}$.

Among which, the surface relaxation time, related to ρ_2 and S/V , is the predominant relaxation time for tight sandstone saturated with liquid; the diffusion relaxation and volume relaxation can be ignored. Therefore, the transverse relaxation time T_2 can be simplified as follows:

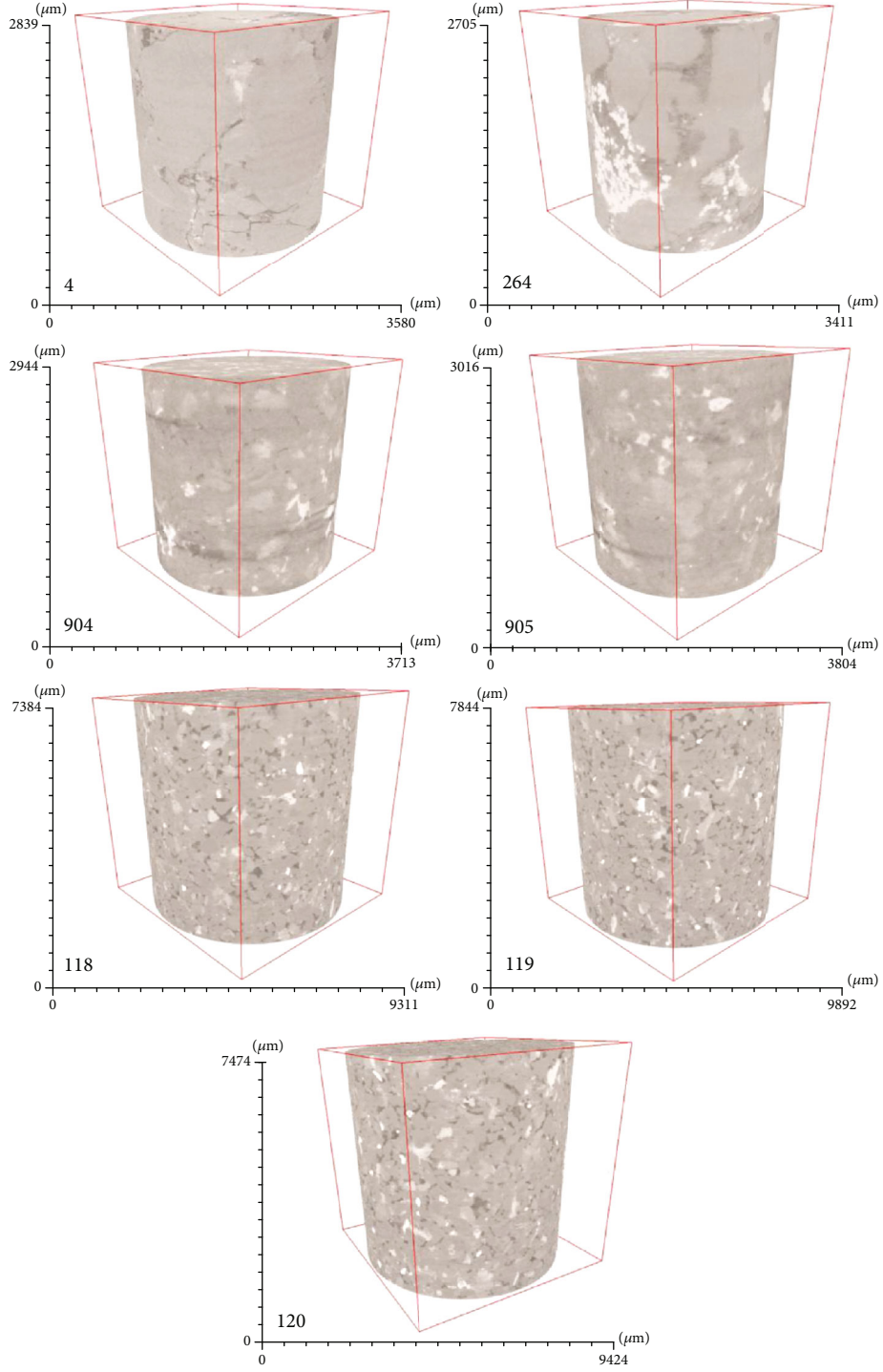


FIGURE 7: The 3D reconstructions of the seven samples.

$$T_2 = \frac{r_c}{\rho_2 F_s}, \quad (6)$$

where F_s represents the pore shape and is equal to 1, 2, or 3 for a slit, cylindrical, or spherical pore, respectively; ρ_2 is related to the relaxing strength of minerals, $\mu\text{m}/\text{ms}$; and r_c is the pore radius, μm .

However, lots of experiments show that the distribution of transverse relaxation time T_2 is a power function with the pore radius r_c as follows [76]:

$$T_2 = \frac{r_c^n}{\rho_2 F_s} = C \cdot r_c^n, \quad (7)$$

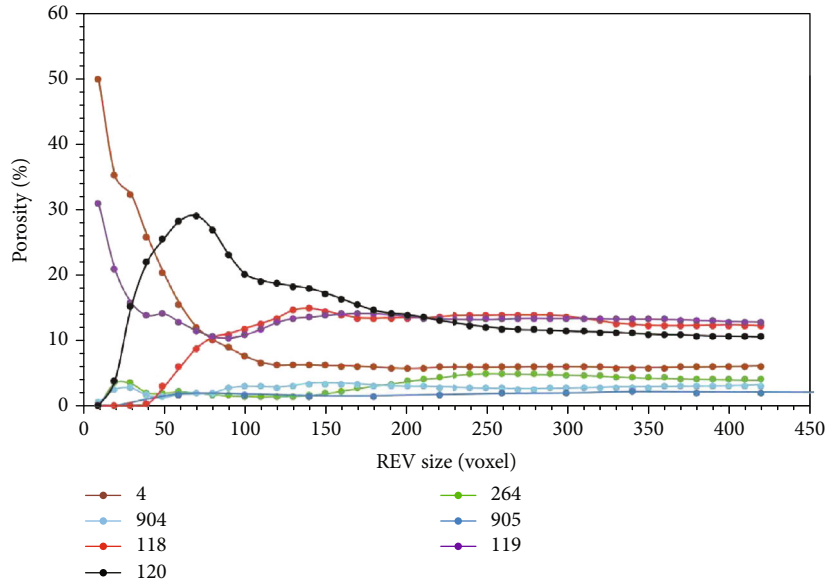


FIGURE 8: REV calculation with the coordinate from the top of the 3D reconstructions.

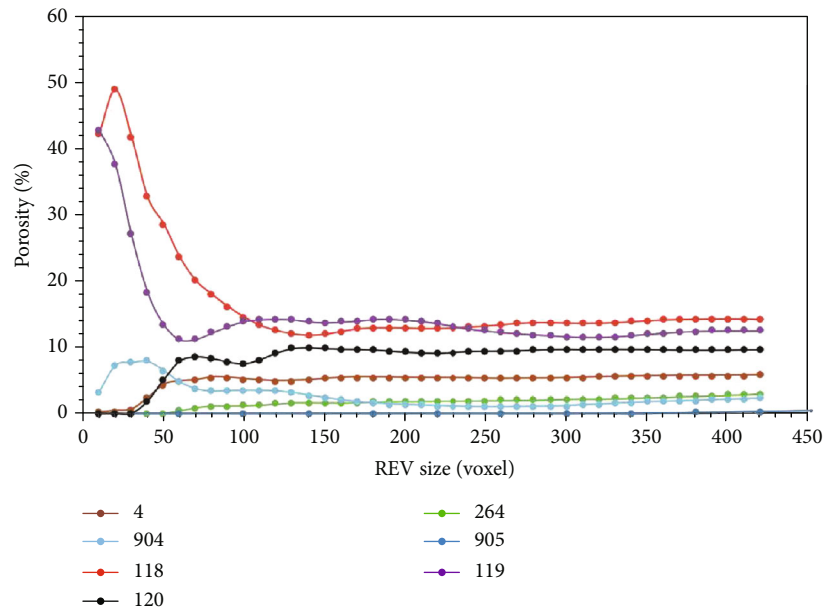


FIGURE 9: REV calculation with the coordinate from the center of the 3D reconstructions.

where the n is power exponent and C equal to $1/\rho_2 F_s$. Fitting the accumulation mercury saturation curve of MICP with the T_2 accumulation distribution curve of NMR, we can get the constant C and power exponent n .

In the 3D digital reconstructed pore body, which was taken from the REV, we determined the pores by the medial axis method, then calculated the equivalent spherical radius by the equivalent sphere method, and due to the resolution of the XCT images, the pores in the reconstructed pore body contain the most large connected pores and isolated pores. The PSD curves derived by the N_2/CO_2 -LPAI, MICP, NMR, and XCT methods are shown in Figure 11.

For the PSD curves derived from N_2 -LPAI, both the adsorption curve and desorption curve can be used to calculate the pore size; but only with an H1 type hysteresis loop, the PSD calculated by desorption curves is accurate [39]. The PSD of sample 120 derived from N_2 -LPAI shown in Figure 11(a) is significantly different from other samples in the macropore range, and its pore volume in the macropore range is larger than any other samples. The reason for this phenomenon may be the defect of the BJH method, because when the relative pressure is higher there is no capillary condensation in macropores [77]. So, the PSD derived from N_2 -LPAI is not suitable to describe the distribution of

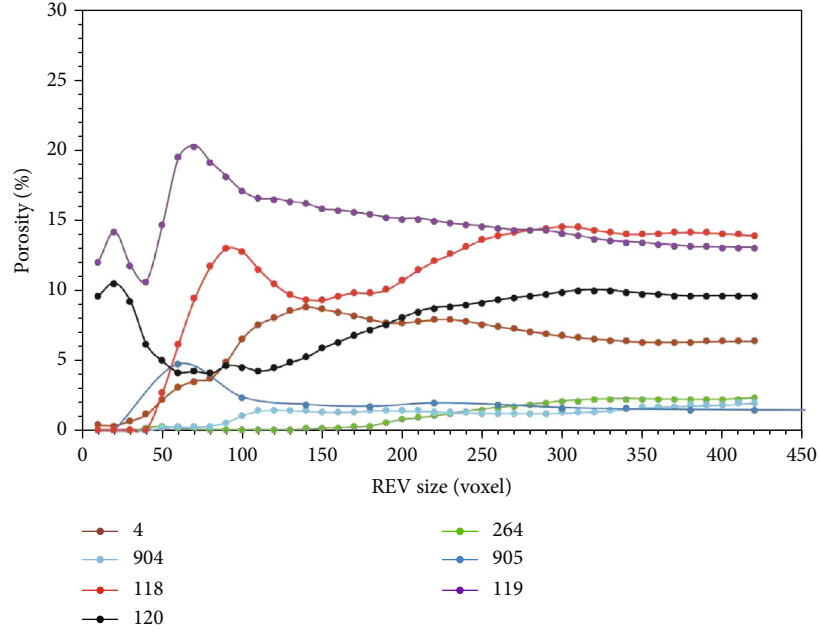


FIGURE 10: REV calculation with the coordinate from the bottom of the 3D reconstructions.

macropores, but it has no effect on the result for the integration of the full PSD.

The PSD curves calculated by the NLDFT method indicate that the micropore width is predominantly $0.0004\ \mu\text{m}$ to $0.001\ \mu\text{m}$ shown in Figure 11(b). The micropore volume of the samples is very small. The PSD curves calculated by the NLDFT method are calculated by the adsorption curves. And the pore volume in the micropore range for samples 904 and 905 is the smallest, and the pore volume in the micropore range for samples 4, 264, 118, 119, and 120 is pretty larger. And some correlation has existed between the micropore pore volume and clay content.

The PSD curve derived by MICP shows a pore volume distribution controlled by pore throats [78]. Therefore, the PSD curves of all seven samples, calculated by the Washburn equation according to the MICP data (shown in Figure 11(c)), show that the PSD curves of the samples with nearly identical clay content have almost the same PSD range (samples 4, 264, 118, 119, and 120). Samples 904 and 905, which have the lowest porosity and permeability, have the smallest pore volume among all the samples. The PSD curves of the Xujiahe formation samples (118, 119, and 120) are almost coincident because of the similar clay type and content.

Due to the correlation between the MICP and T_2 distributions, the transverse relaxation time T_2 can be translated into an equivalent radius of pores, and the signal amplitude corresponds to the volume of the pores. The PSD curves translated from NMR data are shown in Figure 11(d), and the shape of NMR-derived PSD curves is similar to the MICP distribution.

The PSD curves of tight sandstones obtained from XCT are different from the PSD curves from other methods, such as MICP and NMR (shown in Figure 11(e)). From the XCT, there are a great number of small pores, but the total volume

of small pores is relatively low, whereas the large pores show the opposite relationship. The PSD curves from XCT cannot describe pores smaller than the image resolution.

4. Discussion

4.1. Integration of the PSD from Multiple Methods. As stated above, every method has its limitations when describing the PSD of tight sandstones, but a wide PSD is a major characteristic for tight sandstones, so using only each single experiment is insufficient. The integration of different techniques, such as N_2 -LPAI, MICP, NMR, XCT, and NLDFT, is an effective method to determine the full PSD of tight sandstones accurately and effectively.

In the N_2 -LPAI and NLDFT experiments, the pore sizes range from $0.002\ \mu\text{m}$ to $0.2\ \mu\text{m}$ and $0.0004\ \mu\text{m}$ to $0.002\ \mu\text{m}$, respectively, and the pore size range of XCT depends on the resolution of the instrument. The minimum pore size for MICP relies on the maximum pressure of the mercury injection apparatus, about several nanometers. In contrast, the NMR experiment delivers information on pore sizes from several nanometers and several hundred microns. Thus, there is an overlapping range among N_2 -LPAI, NLDFT, XCT, MICP, and NMR data, making it necessary to determine the POCs between these techniques.

There are three different forms of PSD data presentation: differential pore volume versus pore diameter (dV/dR), incremental pore volume versus diameter (dV), and the log differential pore volume versus pore diameter ($dV/d\log R$) [79]. The different forms of PSD data presentation could affect the pore size description and eventually discrepancy derived from the difference of the mathematical forms of these three equations. Each form of PSD data presentation could demonstrate various types of important pore information. There is no difference between the value of dV in large

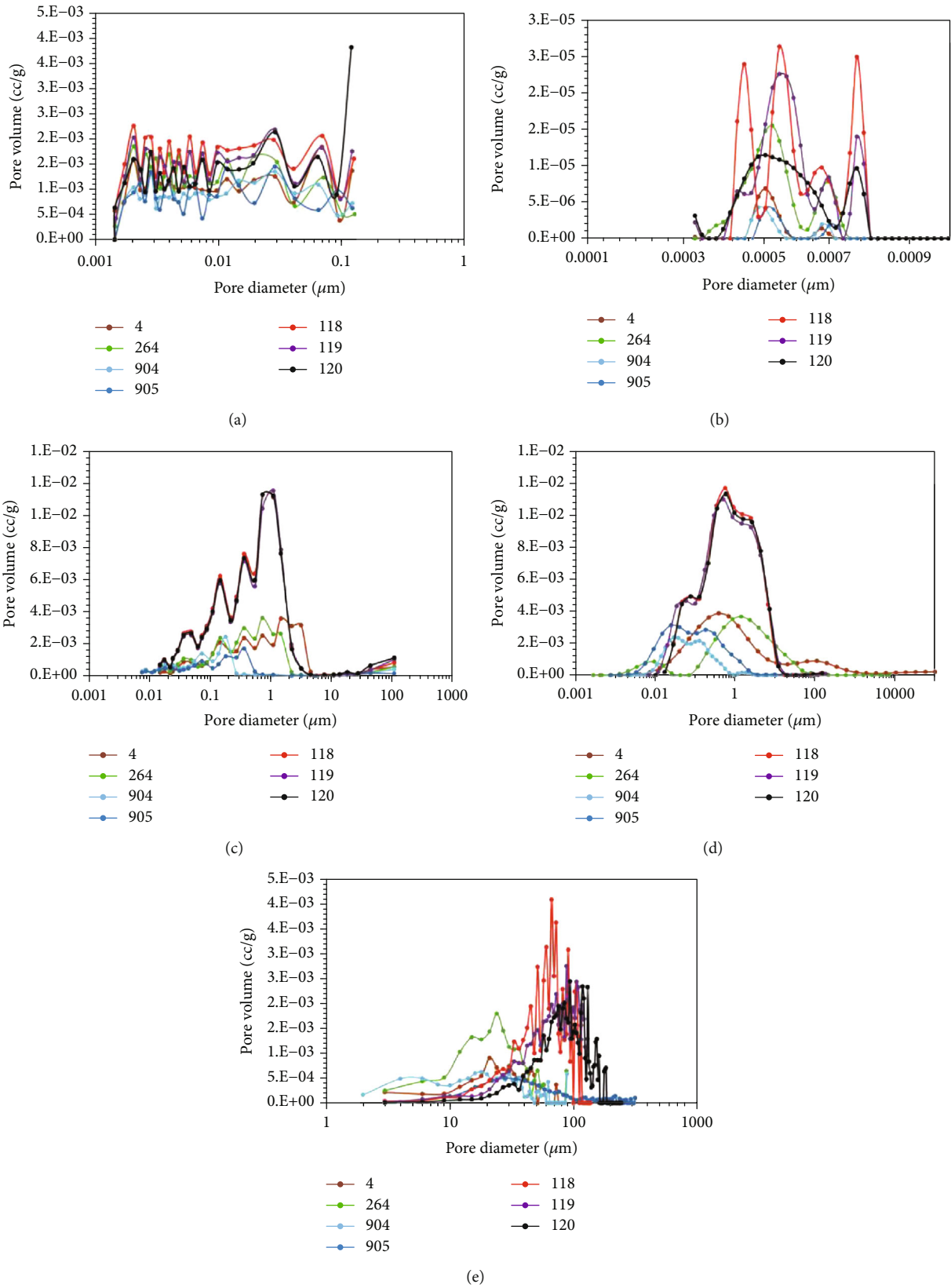


FIGURE 11: Comparison of the PSD curves derived from N₂/CO₂-LPAI, MICP, NMR, and XCT of seven tight sandstones. (a) PSD curves derived from N₂-LPAI. (b) PSD curves derived from CO₂-LPAI. (c) PSD curves derived from MICP. (d) PSD curves derived from NMR. (e) PSD curves derived from XCT.

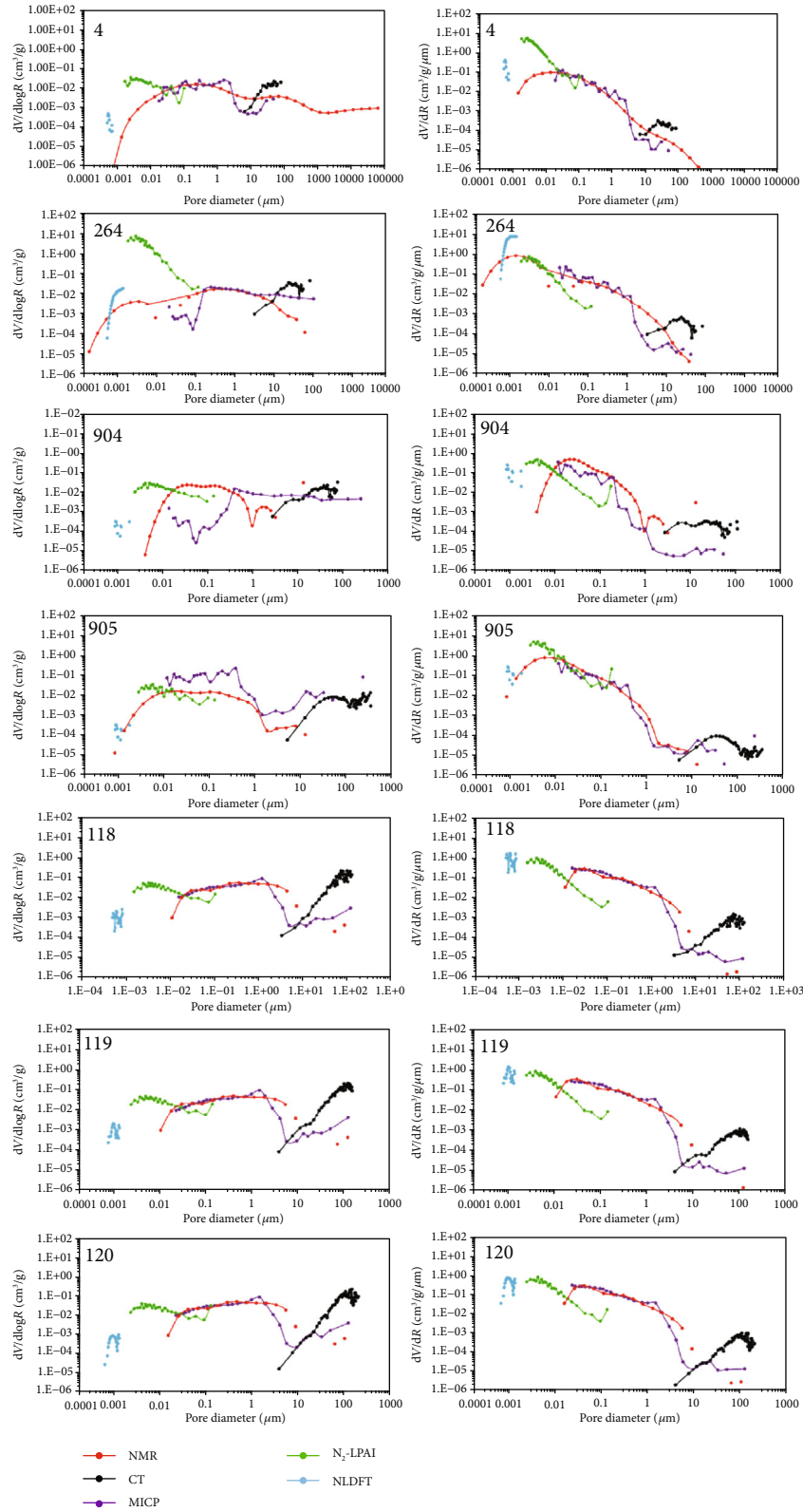


FIGURE 12: Comparison of the $dV/d\log R$ curves and dV/dR curves data presentation.

pore interval and small pore interval; the value of dV/dR in a large pore interval is much less than the volume of dV/dR in a small pore interval; the value of the $dV/d\log R$ is greater than the value of dV/dR in a large pore interval, while it is

opposite in the small pore interval. So, to get a more accurate POC between different PSD curves, the form of dV/dR PSD data presentation could incite the existence of a small pore range, which is more suitable to determine the POC in

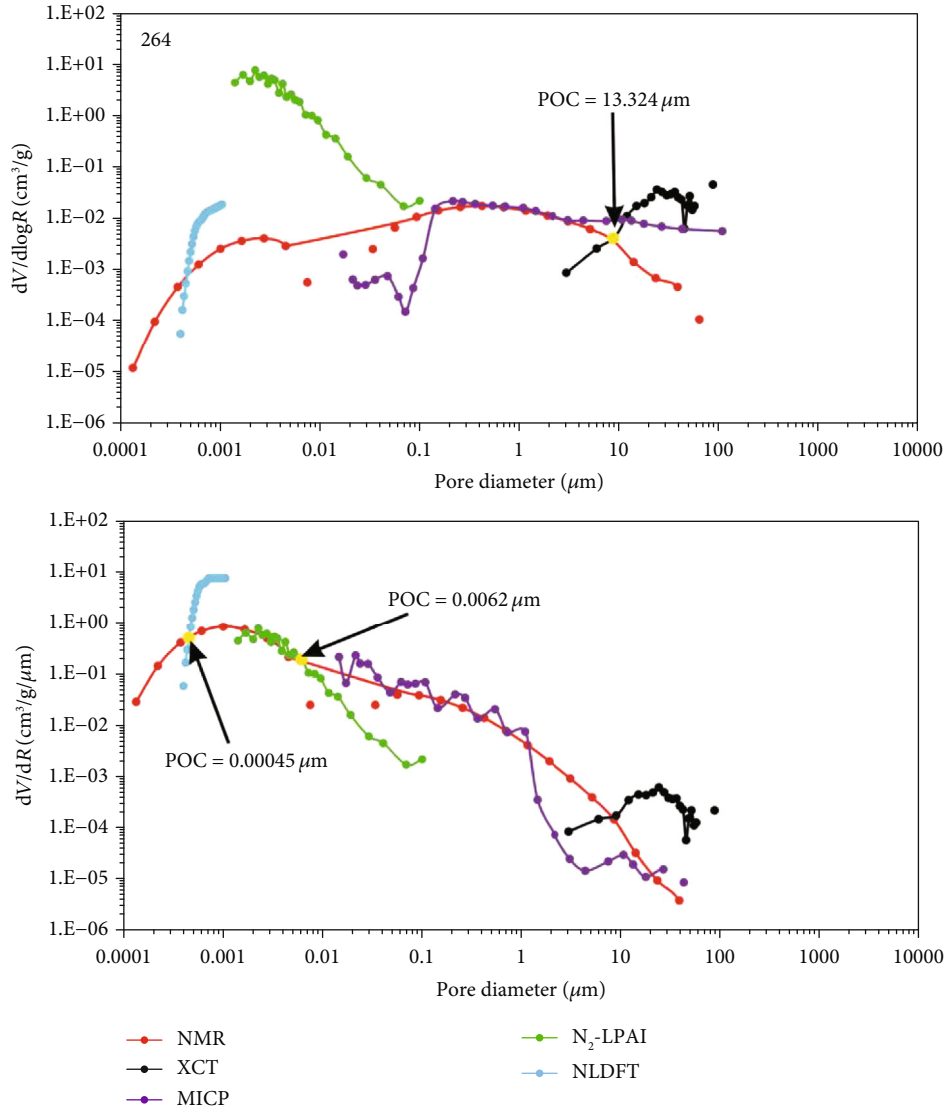


FIGURE 13: Determination of POC in terms of the dV/dR and $dV/d\log R$ curves from sample 264.

smaller pore range, while the form of $dV/d\log R$ PSD data presentation would embolden a large pore range, which can be used to determine the POC in larger pore range. The dV/dR curves and $dV/d\log R$ curves of N_2/CO_2 -LPAI, MICP, NMR, and XCT are shown in Figure 12.

For the full integrated PSD of tight sandstones, choosing the right part of PSD curves derived from different methods between different POCs is critical. The POCs among the N_2 -LPAI, NLDFT, and NMR methods determined by the dV/dR curves could be used to get the full PSD in the small pore range. For the POC determined between NLDFT and NMR, for the left side of PSD, we choose the PSD of NMR and the right side of PSD is NLDFT; if this POC is inexistent, we choose the whole PSD of NLDFT. For the POC determined by N_2 -LPAI and NMR, for the left side of PSD, we choose the PSD of N_2 -LPAI and the right side of PSD is NMR. The $dV/d\log R$ curves could be used to get the POC in the large pore range. And the PSD of the MICP and NMR is nearly the same, so we only choose the XCT curve

and NMR curve to determine the POC in the large pore range. For the POC determined by NMR and XCT, for the left side of PSD, we choose the PSD of NMR and the right side of PSD is XCT. And a representative sample (sample 264) to determine the POCs between different PSD curves is shown in Figure 13.

The full PSD curves of the seven tight sandstones determined by the proposed method are shown in Figure 14. The POC of the N_2 -LPAI, NLDFT, MICP, and XCT methods with NMR can be determined from Figure 12. The porosities from the full PSD curves are evidently greater than the individual PSD curves from N_2 -LPAI, MICP, NLDFT, XCT, and NMR. For tight sandstones, the full PSD curves exhibit massive heterogeneity, and there is an obvious correlation between clay mineral types and full PSD curves of all the samples. The PSD curves of samples 118, 119, and 120 are mainly distributed in the range $0.1 \mu\text{m}$ to $10 \mu\text{m}$, and these PSD curves are relatively uniform, with similar shape and pore size range. The PSD curves of samples 4 and 264 show

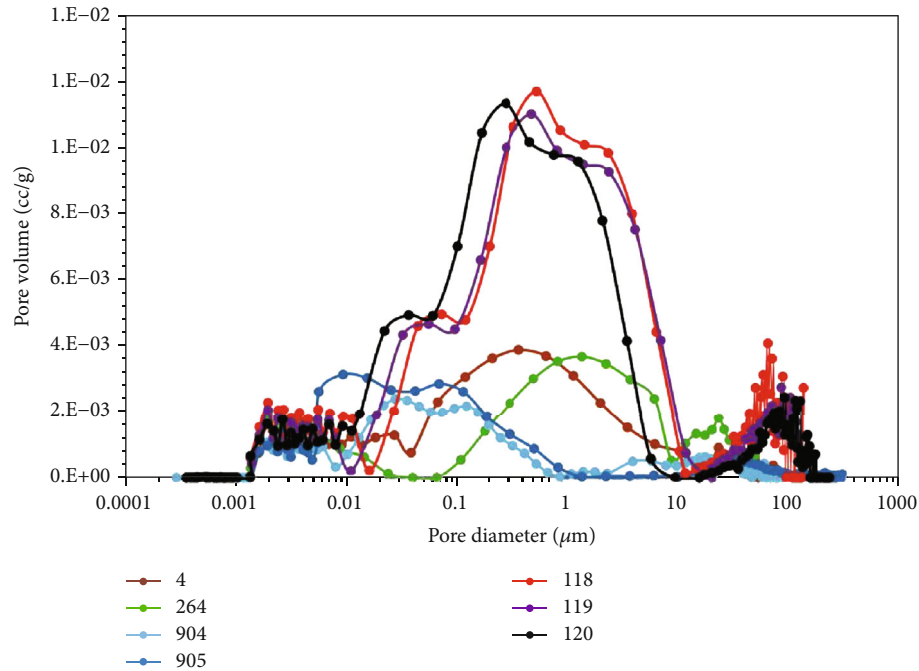


FIGURE 14: Full PSD curves by integration of N_2 -LPPI, NLDFT, XCT, and NMR for the seven tight sandstones.

that these samples are heterogeneous, which have many small pores (range from $0.001 \mu\text{m}$ to $0.1 \mu\text{m}$) and a large proportion of large pores (range from $0.1 \mu\text{m}$ to $10 \mu\text{m}$). The PSD curves of samples 904 and 905, which have the smallest pore size range and lowest pore volume, and most of the pores are less than $0.1 \mu\text{m}$, which is probably the reason why these samples have the lowest permeability and porosity.

4.2. PSD of Tight Sandstones with Different Clay Type. The main classification of pores for tight sandstone is the IUPAC [71], micropores (less than 2 nm), mesopores ($2\text{-}50 \text{ nm}$), and macropores (greater than 50 nm). And this classification scheme of the pore types is based on the pore size, which is not very suitable for tight sandstones. Firstly, the full PSD curves of the tight sandstone are extremely heterogeneous, and the percentage of the micropores and mesopores in IUPAC classification for the full PSD is very small, while the macropores is on the opposite. Recently, some researchers have considered the pore shape and the rock matrix to classify the pore types [80, 81]. But this kind of classification approach does not account for the relationship between clay minerals and pore types.

In order to analyze the PSD features of different clay-rich tight sandstone and to reveal the effect of clay mineral on the PSD, according to the full PSD curves and the pores observed by the SEM images in the tight sandstones, pores are classified into three types: intercrystalline pores (less than $0.01 \mu\text{m}$), clay-related pores and residual intergranular pores ($0.01 \mu\text{m}$ to $10 \mu\text{m}$), and microfractures and dissolution pores (greater than $10 \mu\text{m}$). According to the integrated full PSD curves shown in Figure 14, the relative proportions of different pore types in tight sandstones were calculated (Figure 15).

The pores in pore type I are mainly the intercrystalline pores, which is related to the clay type and the diagenesis. The intercrystalline pores in samples 4 and 264 are mainly generated by the kaolinite crystal, and the intercrystalline pores in samples 904, 905, 118, 119, and 120 are mainly formed by quartz. The pore type I ratios in kaolinite-rich samples 4 and 264 are larger than the ratios in illite-rich samples 904 and 905, and the ratios of illite-rich samples 904 and 905 are larger than the ratios in chlorite-rich samples 118, 119, and 120. On the other hand, the connectivity and porosity for these three types of samples have little relation to the pore type I ratio.

The pores in pore type II comprise the clay-related pores and residual intergranular pores, and this kind of pores is the major pore volume in different clay-rich tight sandstones. The pores of pore type II in samples 4 and 264 are mainly residual intergranular pores. The pores of pore type II in samples 904 and 905 mainly contain clay-related pores, and the fibrous illite will fill the intergranular pores, which can produce this kind of pores. The pores of pore type II in samples 118, 119, and 120 mainly contain clay-related pores and residual intergranular pores; the form of chlorite can produce ubiquitous clay-related pores and protect the primary pores from damage, which can lead to abnormal porosity. The pores of pore type II are the main pores in the tight sandstone whatever the clay minerals are, and this kind of pores has no obvious relation to the connectivity and porosity, too.

The pores in pore type III contain microfractures and dissolution pores, and this kind of pores is typically controlled by the diagenesis. The pore volume ratios of pore type III are different for different clay-rich tight sandstones. The pore volume ratios in chlorite-rich samples 118, 119, and 120 are the largest, the pore volume ratios in kaolinite-rich samples

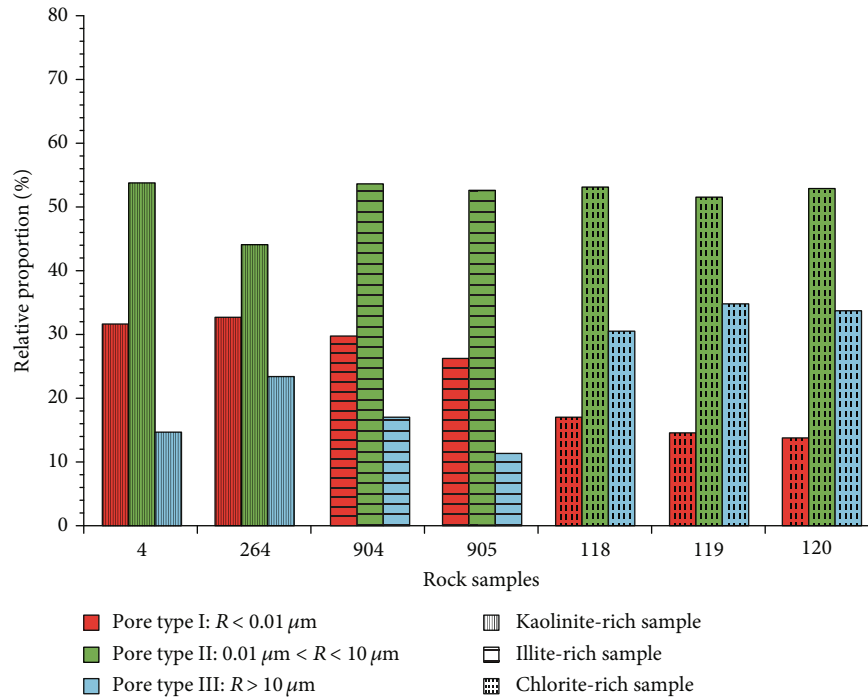


FIGURE 15: Comparison of different types of pore volume from different tight sandstones.

4 and 264 are the second, and the ratios of illite-rich samples 904 and 905 are the smallest. The pore volume ratios of pore type III are related to the connectivity and porosity of tight sandstone samples, and pores of pore type III are mainly distributed in the PSD curves taken from XCT. Due to the resolution of the XCT images, the pores of reconstructed pore body mainly contain the microfractures, dissolution pores, isolated pores, and a part of the residual intergranular pores, so the size of pore taken from XCT is pretty large.

For the full PSD curves of three different kinds of tight sandstones, the pores are dominated by the pore type II (clay-related pores and residual intergranular pores), and the pore volume ratio of pore type I (intercrystalline pores) and pore type III (microfractures and dissolution pores) are both less than 40%. For the kaolinite-rich samples and illite-rich samples, the change of the pore volume ratio of pore type I has little relation to the porosity and connectivity; this indicated that the some small pores may be throats with effect on permeability. On the contrary there is a strong correlation between pore type III and porosity and connectivity, especially the connectivity. This kind of pores are the main connection channels, so a little change of the main connection channels will have a great effect on the permeability of the tight sandstones (Figure 14 and Table 1).

5. Conclusions

SEM, N_2 -LPAI, MICP, XCT, NLDFT, and NMR analyses were performed to reveal pore structure characteristics of tight sandstones collected from different clay-rich samples. A more accurate method to integrate the full PSD for tight

sandstones is proposed. Then, the full PSD curves of different clay-rich samples are analyzed. The primary conclusions from this study are the following:

- (1) According to SEM images, the pores in the kaolinite-rich samples are mainly intercrystalline pores and dissolution pores, the pores in the illite-rich samples are mainly clay-related pores, and the pores in the chlorite-rich samples are mainly clay-related pores, microfractures, and residual intergranular pores
- (2) The form of dV/dR PSD data presentation could incite the existence of a small pore range, which is more suitable to determine the POC in smaller pore range, while the form of $dV/d\log R$ PSD data presentation would embolden a large pore range, which can be used to determine the POC in larger pore range
- (3) According to the full PSD curves and the pores observed by SEM in the tight sandstones, pores are classified into three types: intercrystalline pores (less than $0.01 \mu\text{m}$), clay-related pores and residual intergranular pores ($0.01 \mu\text{m}$ to $10 \mu\text{m}$), and microfractures and dissolution pores (greater than $10 \mu\text{m}$)
- (4) The change of the percentage of intercrystalline pores has little relation to the porosity and connectivity. While there is a strong correlation between microfractures, dissolution pores, porosity, and especially the connectivity. This kind of pores are the main connection channels, so a little change of the main connection channels will have a great effect on the permeability of the tight sandstones

Data Availability

The data used to support the findings of this study have not been made available because the data also forms part of an ongoing study.

Conflicts of Interest

The authors declared that they have no conflicts of interest to this work. We declare that we do not have any commercial or associative interest that represents a conflict of interest in connection with the work submitted.

Acknowledgments

This work was supported by the National Natural Science Foundation of China (Key Program) (Grant No. 51534006), the National Natural Science Foundation of China (Grant Nos. 51874251, 51674211, and 51704247), the PetroChina Innovation Foundation (No. 2018D-5007-0218), and the 111 Project (No. D18016).

References

- [1] Y. Zhang, J. Zeng, Z. Dai et al., "Experimental investigation on oil migration and accumulation in tight sandstones," *Journal of Petroleum Science and Engineering*, vol. 160, pp. 267–275, 2018.
- [2] Y. Zhou, Y. Ji, L. Xu et al., "Controls on reservoir heterogeneity of tight sand oil reservoirs in Upper Triassic Yanchang formation in Longdong area, Southwest Ordos Basin, China: implications for reservoir quality prediction and oil accumulation," *Marine and Petroleum Geology*, vol. 78, pp. 110–135, 2016.
- [3] J. Lai, G. Wang, S. Wang et al., "Review of diagenetic facies in tight sandstones: diagenesis, diagenetic minerals, and prediction via well logs," *Earth-Science Reviews*, vol. 185, pp. 234–258, 2018.
- [4] R. Rezaee, A. Saeedi, and B. Clennell, "Tight gas sands permeability estimation from mercury injection capillary pressure and nuclear magnetic resonance data," *Journal of Petroleum Science and Engineering*, vol. 88–89, pp. 92–99, 2012.
- [5] K. W. Shanley and R. M. Cluff, "The evolution of pore-scale fluid-saturation in low-permeability sandstone reservoirs," *AAPG Bulletin*, vol. 99, no. 10, pp. 1957–1990, 2015.
- [6] C. W. Spencer, "Geologic aspects of tight gas reservoirs in the Rocky Mountain region," *Journal of Petroleum Technology*, vol. 37, no. 7, pp. 1308–1314, 2013.
- [7] R. C. Surdam, "A new paradigm for gas exploration in anomalously pressured "tight gas sands" in Rocky Mountain Laramide basins," *Memoir - American Association of Petroleum Geologists*, vol. 67, pp. 283–298, 1997.
- [8] C. Zou, R. Zhu, K. Liu et al., "Tight gas sandstone reservoirs in China: characteristics and recognition criteria," *Journal of Petroleum Science and Engineering*, vol. 88–89, pp. 82–91, 2012.
- [9] J. Lai, G. Wang, Z. Fan et al., "Insight into the pore structure of tight sandstones using NMR and HPMI measurements," *Energy & Fuels*, vol. 30, no. 12, pp. 10200–10214, 2016.
- [10] R. J. Weger, G. P. Eberli, G. T. Baechle, J. L. Massaferro, and Y. F. Sun, "Quantification of pore structure and its effect on sonic velocity and permeability in carbonates," *AAPG Bulletin*, vol. 93, no. 10, pp. 1297–1317, 2009.
- [11] C. H. Sondergeld, K. E. Newsham, J. T. Comisky, M. C. Rice, and C. S. Rai, "Petrophysical considerations in evaluating and producing shale gas resources," in *SPE Unconventional Gas Conference*, Pittsburgh, Pennsylvania, USA, 2010.
- [12] C. R. Clarkson, M. Freeman, L. He et al., "Characterization of tight gas reservoir pore structure using USANS/SANS and gas adsorption analysis," *Fuel*, vol. 95, pp. 371–385, 2012.
- [13] J. Lai, G. Wang, Z. Wang et al., "A review on pore structure characterization in tight sandstones," *Earth-Science Reviews*, vol. 177, pp. 436–457, 2018.
- [14] W. Li, S. Lu, H. Xue, P. Zhang, and Y. Hu, "Microscopic pore structure in shale reservoir in the argillaceous dolomite from the Jiangnan Basin," *Fuel*, vol. 181, pp. 1041–1049, 2016.
- [15] J. W. Neasham, "The morphology of dispersed clay in sandstone reservoirs and its effect on sandstone shaliness, pore space and fluid flow properties," in *SPE Annual Fall Technical Conference and Exhibition*, Denver, Colorado, 1977.
- [16] L. M. Anovitz and D. R. Cole, "Characterization and analysis of porosity and pore structures," *Reviews in Mineralogy and Geochemistry*, vol. 80, no. 1, pp. 61–164, 2015.
- [17] H. Deng, X. Hu, H. A. Li, B. Luo, and W. Wang, "Improved pore-structure characterization in shale formations with FESEM technique," *Journal of Natural Gas Science and Engineering*, vol. 35, pp. 309–319, 2016.
- [18] M. Abunowara, M. A. Bustam, S. Sufian, and U. Eldemerdash, "Description of carbon dioxide adsorption and desorption onto Malaysian coals under subcritical condition," *Procedia Engineering*, vol. 148, pp. 600–608, 2016.
- [19] B. Nie, X. Liu, L. Yang, J. Meng, and X. Li, "Pore structure characterization of different rank coals using gas adsorption and scanning electron microscopy," *Fuel*, vol. 158, pp. 908–917, 2015.
- [20] H. Wang, R. Rezaee, and A. Saeedi, "Evaporation process and pore size distribution in tight sandstones: a study using NMR and MICP," *Procedia Earth and Planetary Science*, vol. 15, pp. 767–773, 2015.
- [21] L. Zhang, S. Lu, D. Xiao, and B. Li, "Pore structure characteristics of tight sandstones in the northern Songliao Basin, China," *Marine and Petroleum Geology*, vol. 88, pp. 170–180, 2017.
- [22] P. B. Basan, B. D. Lowden, P. R. Whattler, and J. J. Attard, "Pore-size data in petrophysics: a perspective on the measurement of pore geometry," *Geological Society, London, Special Publications*, vol. 122, no. 1, pp. 47–67, 1997.
- [23] C. Xu and C. Torres-Verdín, "Quantifying fluid distribution and phase connectivity with a simple 3D cubic pore network model constrained by NMR and MICP data," *Computational Geosciences*, vol. 61, pp. 94–103, 2013.
- [24] M. E. Curtis, C. H. Sondergeld, R. J. Ambrose, and C. S. Rai, "Microstructural investigation of gas shales in two and three dimensions using nanometer-scale resolution imaging," *AAPG Bulletin*, vol. 96, no. 4, pp. 665–677, 2012.
- [25] S. Hemes, G. Desbois, J. L. Urai, B. Schröppel, and J. O. Schwarz, "Multi-scale characterization of porosity in Boom Clay (HADES-level, Mol, Belgium) using a combination of X-ray μ -CT, 2D BIB-SEM and FIB-SEM tomography," *Microporous and Mesoporous Materials*, vol. 208, pp. 1–20, 2015.
- [26] C. Guo, X. Wang, H. Wang, S. He, H. Liu, and P. Zhu, "Effect of pore structure on displacement efficiency and oil-cluster

- morphology by using micro computed tomography (μ CT) technique,” *Fuel*, vol. 230, pp. 430–439, 2018.
- [27] S. Diamond, “Mercury porosimetry: an inappropriate method for the measurement of pore size distributions in cement-based materials,” *Cement and Concrete Research*, vol. 30, no. 10, pp. 1517–1525, 2000.
- [28] F. Moro and H. Böhni, “Ink-bottle effect in mercury intrusion porosimetry of cement-based materials,” *Journal of Colloid and Interface Science*, vol. 249, no. 1, p. 262, 2002.
- [29] Z. M. Sun, X. C. Lu, X. C. Jia, Y. S. Bai, and W. X. Hu, “Optimization of mercury intrusion capillary pressure measurement for characterizing the pore structure of tight rocks,” *Journal of Nanoscience and Nanotechnology*, vol. 17, no. 9, pp. 6242–6251, 2017.
- [30] Y. Yao and D. Liu, “Comparison of low-field NMR and mercury intrusion porosimetry in characterizing pore size distributions of coals,” *Fuel*, vol. 95, pp. 152–158, 2012.
- [31] J. Zhou, G. Ye, and K. van Breugel, “New mercury porosimetry method for the measurement of pore size distribution in cement-based materials,” in *2nd International RILEM Workshop on Concrete Durability and Service Life Planning (Concrete Life '09)*, Haifa, Israel, 2009.
- [32] E. P. Barrett, L. G. Joyner, and P. P. Halenda, “The determination of pore volume and area distributions in porous substances. I. Computations from nitrogen isotherms,” *Journal of the American Chemical Society*, vol. 73, no. 1, pp. 373–380, 1951.
- [33] G. R. Chalmers, R. M. Bustin, and I. M. Power, “Characterization of gas shale pore systems by porosimetry, pycnometry, surface area, and field emission scanning electron microscopy/transmission electron microscopy image analyses: examples from the Barnett, Woodford, Haynesville, Marcellus, and Doig units,” *AAPG Bulletin*, vol. 96, no. 6, pp. 1099–1119, 2012.
- [34] A. Li, X. Ren, G. Wang, Y. Wang, and K. Jiang, “Characterization of pore structure of low permeability reservoirs using a nuclear magnetic resonance method,” *Journal of China University of Petroleum*, vol. 39, no. 6, pp. 92–98, 2015.
- [35] J. Li, J. Yin, Y. Zhang et al., “A comparison of experimental methods for describing shale pore features — a case study in the Bohai Bay basin of eastern China,” *International Journal of Coal Geology*, vol. 152, pp. 39–49, 2015.
- [36] K. S. W. Sing, “Reporting physisorption data for gas/solid systems with special reference to the determination of surface area and porosity (recommendations 1984),” *Pure and Applied Chemistry*, vol. 57, no. 4, pp. 603–619, 1985.
- [37] S. G. Allen, P. C. L. Stephenson, and J. H. Strange, “Internal surfaces of porous media studied by nuclear magnetic resonance cryoporometry,” *The Journal of Chemical Physics*, vol. 108, no. 19, pp. 8195–8198, 1998.
- [38] M. M. Labani, R. Rezaee, A. Saeedi, and A. A. Hinai, “Evaluation of pore size spectrum of gas shale reservoirs using low pressure nitrogen adsorption, gas expansion and mercury porosimetry: a case study from the Perth and Canning basins, Western Australia,” *Journal of Petroleum Science and Engineering*, vol. 112, pp. 7–16, 2013.
- [39] J. C. Groen, L. A. A. Peffer, and J. Pérez-Ramírez, “Pore size determination in modified micro- and mesoporous materials. Pitfalls and limitations in gas adsorption data analysis,” *Microporous and Mesoporous Materials*, vol. 60, no. 1-3, pp. 1–17, 2003.
- [40] S. Lowell, J. E. Shields, M. A. Thomas, and M. Thommes, *Characterization of Porous Solids and Powders: Surface Area, Pore Size and Density*, vol. 16, Springer Science & Business Media, 2012.
- [41] M. Thommes and K. A. Cychosz, “Physical adsorption characterization of nanoporous materials: progress and challenges,” *Adsorption*, vol. 20, no. 2-3, pp. 233–250, 2014.
- [42] Z. Zhang and Z. Yang, “Theoretical and practical discussion of measurement accuracy for physisorption with micro- and mesoporous materials,” *Chinese Journal of Catalysis*, vol. 34, no. 10, pp. 1797–1810, 2013.
- [43] G. Horváth and K. Kawazoe, “Method for the calculation of effective pore size distribution in molecular sieve carbon,” *Journal of Chemical Engineering of Japan*, vol. 16, no. 6, pp. 470–475, 1983.
- [44] R. Evans, U. M. B. Marconi, and P. Tarazona, “Capillary condensation and adsorption in cylindrical and slit-like pores,” *Faraday Transactions*, vol. 82, no. 10, pp. 1763–1787, 1986.
- [45] C. Lastoskie, K. E. Gubbins, and N. Quirke, “Pore size distribution analysis of microporous carbons: a density functional theory approach,” *The Journal of Physical Chemistry*, vol. 97, no. 18, pp. 4786–4796, 1993.
- [46] P. I. Ravikovitch and A. V. Neimark, “Characterization of nanoporous materials from adsorption and desorption isotherms,” *Colloids and Surfaces, A: Physicochemical and Engineering Aspects*, vol. 187-188, pp. 11–21, 2001.
- [47] N. A. Seaton, J. P. R. B. Walton, and N. Quirke, “A new analysis method for the determination of the pore size distribution of porous carbons from nitrogen adsorption measurements,” *Carbon*, vol. 27, no. 6, pp. 853–861, 1989.
- [48] O. V. Petrov and I. Furo, “NMR cryoporometry: principles, applications and potential,” *Progress in Nuclear Magnetic Resonance Spectroscopy*, vol. 54, no. 2, pp. 97–122, 2009.
- [49] J. H. Strange, M. Rahman, and E. G. Smith, “Characterization of porous solids by NMR,” *Physical Review Letters*, vol. 71, no. 21, pp. 3589–3591, 1993.
- [50] R. M. E. Valckenborg, L. Pel, and K. Kopinga, “Combined NMR cryoporometry and relaxometry,” *Journal of Physics D: Applied Physics*, vol. 35, no. 3, pp. 249–256, 2002.
- [51] J. B. W. Webber, J. H. Strange, and J. C. Dore, “An evaluation of NMR cryoporometry, density measurement and neutron scattering methods of pore characterisation,” *Magnetic Resonance Imaging*, vol. 19, no. 3-4, pp. 395–399, 2001.
- [52] Y. Zhao, Y. Sun, S. Liu, K. Wang, and Y. Jiang, “Pore structure characterization of coal by NMR cryoporometry,” *Fuel*, vol. 190, pp. 359–369, 2017.
- [53] B. Zhou, Q. Han, and P. Yang, “Characterization of nanoporous systems in gas shales by low field NMR cryoporometry,” *Energy & Fuels*, vol. 30, no. 11, pp. 9122–9131, 2016.
- [54] B. Liu, S. Yao, W. Hu, and J. Cao, “Applying octamethylcyclotetrasiloxane as a probe liquid for characterizing the pore size distribution of oil-bearing tight sandstones by nuclear magnetic resonance cryoporometry,” *Marine and Petroleum Geology*, vol. 88, pp. 814–825, 2017.
- [55] E. N. Mbia, I. L. Fabricius, A. Krogsboll, P. Frykman, and F. Dalhoff, “Permeability, compressibility and porosity of Jurassic shale from the Norwegian-Danish basin,” *Petroleum Geoscience*, vol. 20, no. 3, pp. 257–281, 2014.
- [56] E. Rosenbrand, I. L. Fabricius, Q. Fisher, and C. Grattoni, “Permeability in Rotliegend gas sandstones to gas and brine as predicted from NMR, mercury injection and image analysis,” *Marine and Petroleum Geology*, vol. 64, pp. 189–202, 2015.

- [57] N. Bossa, P. Chaurand, J. Vicente et al., "Micro- and nano-X-ray computed-tomography: a step forward in the characterization of the pore network of a leached cement paste," *Cement and Concrete Research*, vol. 67, pp. 138–147, 2015.
- [58] J. Zeng, X. Feng, S. Feng, Y. Zhang, J. Qiao, and Z. Yang, "Influence of tight sandstone micro-nano pore-throat structures on petroleum accumulation: evidence from experimental simulation combining X-ray tomography," *Journal of Nanoscience and Nanotechnology*, vol. 17, no. 9, pp. 6459–6469, 2017.
- [59] J. F. Delerue, S. V. Lomov, R. S. Parnas, I. Verpoest, and M. Wevers, "Pore network modeling of permeability for textile reinforcements," *Polymer Composites*, vol. 24, no. 3, pp. 344–357, 2003.
- [60] D. Denney, "Robust determination of the pore-space morphology in sedimentary rocks," *Journal of Petroleum Technology*, vol. 56, no. 5, pp. 69–70, 2015.
- [61] H. S. Tuan and D. W. Huttmacher, "Application of micro CT and computation modeling in bone tissue engineering," *Computer-Aided Design*, vol. 37, no. 11, pp. 1151–1161, 2005.
- [62] Y. You, X. Niu, Y. Li, X. Yang, and W. Dan, "Application of CT scanning system to study of micro-pore structure of tight sandstone: a case study of Chang-7 member of Yanchang formation in Ordos Basin," *Xinjiang Petroleum Geology*, vol. 37, pp. 227–230, 2016.
- [63] J. M. Kate and C. S. Gokhale, "A simple method to estimate complete pore size distribution of rocks," *Engineering Geology*, vol. 84, no. 1–2, pp. 48–69, 2006.
- [64] D. Xiao, Z. Lu, S. Jiang, and S. Lu, "Comparison and integration of experimental methods to characterize the full-range pore features of tight gas sandstone—a case study in Songliao Basin of China," *Journal of Natural Gas Science and Engineering*, vol. 34, pp. 1412–1421, 2016.
- [65] Z. Zhang, Y. Shi, H. Li, and W. Jin, "Experimental study on the pore structure characteristics of tight sandstone reservoirs in Upper Triassic Ordos Basin China," *Energy Exploration & Exploitation*, vol. 34, no. 3, pp. 418–439, 2016.
- [66] J. Lai, G. Wang, Y. Chai et al., "Deep burial diagenesis and reservoir quality evolution of high-temperature, high-pressure sandstones: examples from lower cretaceous Bashijiqike formation in Keshen area, Kuqa depression, Tarim basin of China," *AAPG Bulletin*, vol. 101, no. 6, pp. 829–862, 2017.
- [67] J. Lai and G. Wang, "Fractal analysis of tight gas sandstones using high-pressure mercury intrusion techniques," *Journal of Natural Gas Science and Engineering*, vol. 24, pp. 185–196, 2015.
- [68] D. Yue, S. Wu, Z. Xu et al., "Reservoir quality, natural fractures, and gas productivity of Upper Triassic Xujiahe tight gas sandstones in western Sichuan Basin, China," *Marine and Petroleum Geology*, vol. 89, pp. 370–386, 2018.
- [69] P. Li, M. Zheng, H. Bi, S. Wu, and X. Wang, "Pore throat structure and fractal characteristics of tight oil sandstone: a case study in the Ordos basin, China," *Journal of Petroleum Science and Engineering*, vol. 149, pp. 665–674, 2017.
- [70] M. Wang, H. Tang, F. Zhao et al., "Controlling factor analysis and prediction of the quality of tight sandstone reservoirs: a case study of the He8 member in the eastern Sulige gas field, Ordos Basin, China," *Journal of Natural Gas Science and Engineering*, vol. 46, pp. 680–698, 2017.
- [71] J. Rouquerol, D. Avnir, C. W. Fairbridge et al., "Recommendations for the characterization of porous solids (technical report)," *Pure and Applied Chemistry*, vol. 66, no. 8, pp. 1739–1758, 1994.
- [72] W. Kewen and L. Ning, "Numerical simulation of rock pore-throat structure effects on NMR T2 distribution," *Applied Geophysics*, vol. 5, no. 2, pp. 86–91, 2008.
- [73] V. Cnudde and M. N. Boone, "High-resolution X-ray computed tomography in geosciences: a review of the current technology and applications," *Earth-Science Reviews*, vol. 123, pp. 1–17, 2013.
- [74] K. Remeysen and R. Swennen, "Application of microfocus computed tomography in carbonate reservoir characterization: possibilities and limitations," *Marine and Petroleum Geology*, vol. 25, no. 6, pp. 486–499, 2008.
- [75] E. W. Washburn, "The dynamics of capillary flow," *Physical Review*, vol. 17, no. 3, pp. 273–283, 1921.
- [76] Z. Q. Mao, Y. D. He, and X. J. Ren, "An improved method of using NMR T2 distribution to evaluate pore size distribution," *Chinese Journal of Geophysics*, vol. 48, no. 2, pp. 412–418, 2005.
- [77] F. Yang, Z. F. Ning, S. D. Zhang, C. P. Hu, L. H. Du, and H. Q. Liu, "Characterization of pore structures in shales through nitrogen adsorption experiment," *Natural Gas Industry*, vol. 33, no. 4, pp. 135–140, 2013.
- [78] C. Lyu, Z. Ning, Q. Wang, and M. Chen, "Application of NMRT2to pore size distribution and movable fluid distribution in tight sandstones," *Energy & Fuels*, vol. 32, no. 2, pp. 1395–1405, 2018.
- [79] K. Meyer and P. Klobes, "Comparison between different presentations of pore size distribution in porous materials," *Fresenius' Journal of Analytical Chemistry*, vol. 363, no. 2, pp. 174–178, 1999.
- [80] R. G. Loucks, R. M. Reed, S. C. Ruppel, and U. Hammes, "Spectrum of pore types and networks in mudrocks and a descriptive classification for matrix-related mudrock pores," *AAPG Bulletin*, vol. 96, no. 6, pp. 1071–1098, 2012.
- [81] R. M. Slatt and N. R. O'Brien, "Pore types in the Barnett and Woodford gas shales: contribution to understanding gas storage and migration pathways in fine-grained rocks," *AAPG Bulletin*, vol. 95, no. 12, pp. 2017–2030, 2011.